



# Nano- and Microscopic Investigation on the Strengthening Mechanism of ITZs Using Waste Glass Powder in Modeled Aggregate Concrete

Hanbing Zhao<sup>1</sup>; Wengui Li<sup>2</sup>; Yixiang Gan<sup>3</sup>; Aziz Hasan Mahmood<sup>4</sup>; Xinyu Zhao<sup>5</sup>; and Kejin Wang<sup>6</sup>

**Abstract:** As a pozzolan, waste glass powder (WGP) can improve the mechanical properties and durability of concrete, especially at a later age. However, the modification mechanisms should be fully understood and discussed. One of the effective approaches is to investigate the improvement in interfacial transition zones (ITZs) between aggregate and mortar matrix. In this paper, soda-lime WGP was used as a supplementary cementitious material and replaced 20% by weight cement in the sample with modeled aggregate. The phases and chemical composition within the ITZs and the adjacent mortar matrix were investigated by backscattered electron (BSE) imaging combined with image analysis. Advanced nanomechanical techniques were simultaneously applied, and the results obtained from nanoindentation and nanoscratch were compared. The results show that WGP can significantly reduce the width of ITZs and increase the content of calcium-silicate-hydrate (C-S-H) and Si/Ca ratio in both ITZs and matrix. The high heterogeneity of ITZ with WGP made it susceptible to errors caused by unreacted WGP during the measurement of C-S-H nano- and micromechanical properties. For the control group without WGP, the test results of nanoindentation and nanoscratch showed a high degree of consistency. However, for the samples with 20% by weight WGP, there are some differences in the test results between nanoindentation and nanoscratch. Nanoscratch was able to acquire abundant data in a short testing time and proved more suitable for the tests of homogeneous materials. On the other hand, for the sample with 20% by weight WGP, nanoindentation was found to more likely to reflect the real micromechanical properties of ITZs based on abundant indentation tests. DOI: 10.1061/JMCEE7.MTENG-16956. © 2024 American Society of Civil Engineers.

**Author keywords:** Waste glass powder (WGP); Modeled aggregate concrete (MAC); Interfacial transition zone (ITZ); Image analysis; Nano- and micromechanical characterization.

## Introduction

Portland cement has long been identified as an energy-intensive material, contributing to 5%–7% of anthropogenic carbon emissions (Tang et al. 2020). To reduce its carbon footprint, the use

of low-carbon supplementary cementitious materials (SCMs) is well-recognized. For instance, Australian Standard (AS) number AS 3972 (AS 2010) increased the allowable proportion of mineral additions (fly ash, slag, and/or limestone) from 5% to 7.5% to permit a reduction in the carbon footprint of cement manufacturing (Mohammadi and South 2016). This limit extends to more than 7.5% of fly ash and/or slag and up to 10% amorphous silica for blended cement (Type GB as per AS 3972). However, popular SCMs such as fly ash are on the decline from the rapid shift from coal-powered power plants to sustainable alternatives, blast furnace slag processing through water quenching is a carbon-intensive process, and silica fume in high volume introduces some challenges to concrete (such as high drying shrinkage). In Australia alone, a total of 1.16 million tons of waste glass was generated between 2018 and 2019 (Dong et al. 2021). As such, alternative SCMs like recycled glass, which are abundant and require reasonable processing, are to be investigated to understand their suitability to be incorporated into the mix.

Researchers successfully crushed waste glass into cullet or sand to recycle them as raw materials for concrete (Ye et al. 2022; Arabi et al. 2019). However, high concentrations of amorphous silica in waste glass could react with alkalis in pore solution and increase the risk of destructive alkali-silica reaction expansion of concrete, which restricts the widespread application of waste glass in cement-based materials (Dong et al. 2021). On the other hand, comprised of around 70% silica, waste glass can perform considerable pozzolanic reactivity when it is further ground into powder lower than 75  $\mu\text{m}$  and can be regarded as a qualified substitute for conventional portland cement (Jiang et al. 2019). Ground glass can also

<sup>1</sup>Ph.D. Candidate, School of Civil and Environmental Engineering, Univ. of Technology Sydney, Sydney, NSW 2007, Australia. Email: hanbing.zhao@student.uts.edu.au

<sup>2</sup>Associate Professor and Australian Research Council (ARC) Future Fellow, School of Civil and Environmental Engineering, Univ. of Technology Sydney, Sydney, NSW 2007, Australia (corresponding author). ORCID: <https://orcid.org/0000-0002-4651-1215>. Email: wengui.li@uts.edu.au

<sup>3</sup>Associate Professor, School of Civil Engineering, Univ. of Sydney, Sydney, NSW 2006, Australia; Associate Professor, Nano Institute, Univ. of Sydney, Sydney, NSW 2006, Australia. Email: yixiang.gan@sydney.edu.au

<sup>4</sup>Lecturer, School of Civil and Environmental Engineering, Univ. of Technology Sydney, Sydney, NSW 2007, Australia. Email: aziz.mahmood@uts.edu.au

<sup>5</sup>Associate Professor, State Key Laboratory of Subtropical Building Science, South China Univ. of Technology, Guangdong 510641, China. Email: ctzhaoxy@scut.edu.cn

<sup>6</sup>Professor, Dept. of Civil, Construction, and Environmental Engineering, Iowa State Univ., Ames, IA 50011. Email: kejinw@iastate.edu

Note. This manuscript was submitted on May 17, 2023; approved on September 8, 2023; published online on January 18, 2024. Discussion period open until June 18, 2024; separate discussions must be submitted for individual papers. This paper is part of the *Journal of Materials in Civil Engineering*, © ASCE, ISSN 0899-1561.

inhibit the alkali-silica reaction (ASR) expansion of glass sand and other reactive aggregates to an acceptable limit set by standards AS 1141.60.1 (AS 2014) and ASTM C1567-13 (ASTM 2013) (Mahmood et al. 2022; Ke et al. 2018).

Similar to conventional SCMs such as fly ash, granulated blast furnace slag, and silica fume, which have been widely used in concrete manufacture, amorphous silica in waste glass is an important raw material for pozzolanic reactions, and with the decrease of particle size of waste glass powder (WGP), the pozzolanic activity tends to be greatly enhanced (Jiang et al. 2019). Mirzahosseini and Riding (2015) found that 0–25  $\mu\text{m}$  WGP possessed a higher specific surface area and exhibited satisfying pozzolanic reactivity as early as the first day. After 25% of the cement was substituted by WGP, the compactness of the calcium-silicate-hydrate (C-S-H) gel and the compressive strength of the samples were significantly improved (Mirzahosseini and Riding 2015).

Most research on the performance of concrete containing WGP still stayed on the macroscopic level, including rheological properties, mechanical properties, and durability (Jiang et al. 2019). Understanding the mechanisms responsible for these behaviors requires more in-depth research at the microscopic level. However, a small amount of research at the microscopic level is limited to simple scanning electron microscopy (SEM) image observation and identification of the changes in chemical elements and mineralogical phase between paste samples with/without WGP (Du and Tan 2017; Pan et al. 2017; Mejdí et al. 2019). In these limited studies, Du and Tan (2017) learned from X-ray diffraction (XRD) and thermogravimetric analysis (TGA) that WGP can effectively consume calcium hydroxide and generate C-S-H gel with a low Ca/Si ratio. Pan et al. (2017) found that the hexagonal plate crystals of portlandite disappeared at a high temperature of 500°C, and the microstructure of the mortar introduced with 20% by weight WGP was less affected by the high temperature because the glass particles consumed portlandite and filled the pores. Although Mejdí et al. (2019, 2022) recently studied the long-term hydration process of cement paste containing glass powder through thermodynamic modeling, XRD-Rietveld analysis, and quantitative element distribution analysis, the investigation of concrete samples made with WGP and its interfacial transition zone (ITZ) is still insufficient, and there is a lack of in-depth analysis of large batches of test data by image analysis and mathematical statistics techniques.

ITZ forms around aggregates and is the weakest region in concrete, which accounts for around 20%–30% of the overall volume. Because most concrete cracks along the ITZ under loading, this is critical in determining the mechanical properties and durability of concrete (Luo et al. 2021). The existing SEM, nanoindentation, and nanoscratch techniques combined with image analysis and statistical knowledge are a more effective scientific approach toward exploring the modification mechanism of SCMs on the microscopic properties of concrete. These techniques can visually and quantitatively explain how SCMs modify ITZ. In the study by Golewski (2018), 20% fly ash additive reduced the crack width within ITZs, and thereby, the concrete sample with fly ash was characterized by low permeability and higher durability. Through SEM, energy dispersive X-ray spectroscopy (EDS), and nanoindentation techniques, Hosan et al. (2021) found that nano  $\text{SiO}_2$  and nano  $\text{CaCO}_3$  can increase the content of Ca, Si, and Al element ratios in ITZ, reducing the width of ITZ, making the microstructure more compact, and enhancing the micromechanical properties of ITZ. Xu et al. (2017) also found that nano  $\text{SiO}_2$  can accelerate hydration and improve the elastic modulus and hardness of ITZs. The nanoindentation test results were reasonably correlated to the macroscopic mechanical properties (Xu et al. 2017). However, mechanisms of WGP for improved mechanical properties and durability, possibly from an improved ITZ, remain unexplored.

In addition, the existing literature shows that researchers usually tested the micromechanical properties of ITZ by nanoindentation (Xiao et al. 2013a; Li et al. 2012). As a traditional technique, the advantages of nanoindentation for testing the micromechanical properties of materials have been fully proved in many experiments (Xiao et al. 2013b; Li et al. 2012). However, for highly heterogeneous concrete materials, nanoindentation is not only time-consuming but also highly susceptible to localized effects (Li et al. 2021). In comparison, nanoscratch can obtain uniform and continuous ITZ micromechanical performance test results in a relatively shorter duration, but it has not been utilized in concrete ITZ studies (Li et al. 2021). In the few related studies, most research was focused on cement-based paste or geopolymer composite, and the influence of test parameters on the nanoscratch results (Hoover and Ulm 2015; Akono and Ulm 2017; Wei et al. 2021).

Therefore, a multitechnique holistic investigation approach including image analysis, chemical phase quantitative analysis, and micromechanical tests were combined with statistical techniques to explore the changes in ITZs from the inclusion of WGP in this study. To minimize the interference of inhomogeneity of materials on test results, a simplified ITZ was simulated by modeled aggregate concrete (MAC). The efficiency and accuracy of MAC in the study of ITZs have been demonstrated in previous studies (Fu et al. 2020; Zhan et al. 2020; Xiao et al. 2013a). Two pieces of natural granite stones were ground into blocks and covered with pure-cement mortar and mortar containing 20% WGP, respectively. The modification efficiency of WGP on concrete ITZs was evaluated from test results.

## Experimental Program and Analysis Methods

### Raw Materials

General-purpose portland cement (GP cement) conforming to AS 3972 was the main cementitious material in this study. Waste glass (soda-lime glass), preliminary composed of recycled municipal curbside council collection, was milled to fine powder by a mill machine (Fig. 1) in the laboratory to replace 20% by weight of cement as SCM. The particle size distribution (PSD) curves of cement and WGP measured by a Malvern Mastersizer 3000 (Malvern Panalytical Ltd., Malvern, UK) are shown in Fig. 2.

The WGP was ground to achieve a similar PSD to cement with a median particle size of  $\sim 20 \mu\text{m}$ . The detailed chemical compositions determined using X-ray fluorescence (XRF) are presented in Table 1. The loss on ignition (LOI) of WGP in Table 1 suggests that before supply, the glass fragments went through a furnace at a high temperature to reduce the organic content and residuals (liquid and paper tags) to a minimum. The main oxide components of cement and WGP were calcium oxide and silica, respectively. Each MAC contained a granite block as natural coarse aggregate, ground from the single aggregate particle. Naturally occurring silica sand with a fineness modulus of 1.9 was selected as the fine aggregate.

### Sample Preparation

Modeled concrete samples were made by placing a piece of aggregate into the mortar. The mortar had a water-cement ratio of 0.45 and a sand-cement ratio (by mass) of 1.5. In one group of samples, 100% cement was used, whereas in the other, 20% by weight of cement was replaced by WGP. Following previous research on modeled samples (Luo et al. 2021, 2022; Li et al. 2021), the MAC processing steps were designed and are shown in Fig. 3.

Firstly, the granite gravel with a suitable size was selected and ground to a  $13 \times 13 \times 8\text{-mm}$  block. The granite block was further

ground using a series of abrasive paper with different grits for 30 min and polished by 0.3 and 0.05  $\mu\text{m}$  alumina slurries for 20 min. The alumina particles attached to the surface of the granite were removed in an ultrasonic bath. Subsequently, the surfaced-dried



Fig. 1. Mill machine for waste glass.

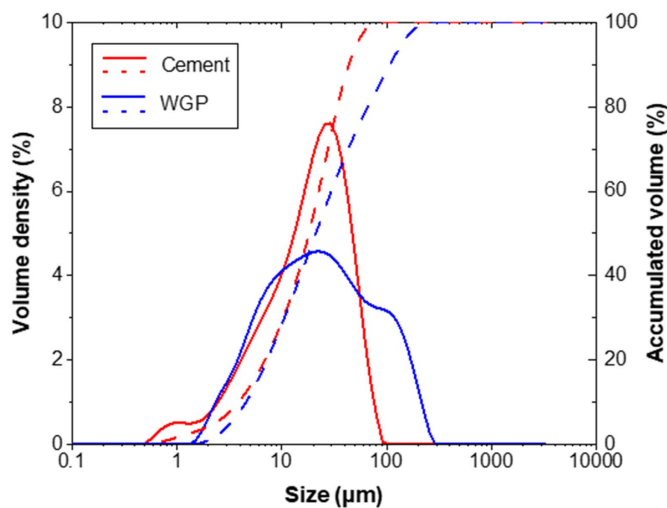


Fig. 2. Particle size distribution of cement and WGP.

Table 1. Chemical composition of cement and WGP

| Materials | CaO  | SiO <sub>2</sub> | Al <sub>2</sub> O <sub>3</sub> | SO <sub>3</sub> | Fe <sub>2</sub> O <sub>3</sub> | MgO | K <sub>2</sub> O | Na <sub>2</sub> O | LOI |
|-----------|------|------------------|--------------------------------|-----------------|--------------------------------|-----|------------------|-------------------|-----|
| Cement    | 64.9 | 18.6             | 4.1                            | 3.0             | 3.1                            | 1.6 | 0.5              | —                 | 4.2 |
| WGP       | 10.8 | 68.4             | 0.9                            | 0.1             | 0.4                            | 1.8 | 0.3              | 13.5              | 3.8 |

Note: LOI = loss on ignition.

granite block was put in a  $\text{Ø}35\text{-mm}$  cylindrical mold and poured with fresh mortar. Large air bubbles were discharged by tapping. After curing in the mold for 1 day and being transferred and stored in a water tank at  $23^\circ\text{C} \pm 3^\circ\text{C}$  for 3 months, the semifinished sample was briefly ground and covered with a layer of epoxy resin to avoid damage to the ITZ during the following cutting.

The sample that was cut and exposed to the ITZ was recovered with a layer of epoxy resin in a  $\text{Ø}35\text{ mm}$  cylindrical mold. After the observation side was ground for 30 min and polished for 40 min, the sample was put in an ultrasonic bath for 2 min to remove alumina particles on the surface. Finally, the samples were put in a vacuum drying oven at  $40^\circ\text{C}$  for 2 days. The MAC covered with epoxy resin was subjected to nanoindentation, nanoscratch, and backscattered electron-energy dispersive spectrometer (BSE-EDS) tests. Then, the mortar on the MAC was cut out and ground into powder for XRD and Fourier transform infrared spectroscopy (FTIR) tests. Although it is impossible to accurately measure the change of the mineral phase and chemical composition within ITZs, the pozzolanic reaction and its influence on the properties of ITZ with WGP was reasonably inferred through the analysis of the chemical composition differences between mortar matrix in MAC with and without WGP.

## Experimental Methods

### Microstructure Examination and Analysis

To improve conductivity of concrete samples, the surface was coated with 5 nm of gold. Thirty BSE images with a magnification of  $500\times$  were randomly extracted from the ITZs with and without WGP along the lateral boundary of the granite block. The probe current and accelerating voltage were set to 875 pA and 15 kV, respectively. The working distance was around 10 mm. To reduce unnecessary workload in subsequent analysis, the brightness and contrast during the observation process were kept consistent.

For statistical analysis of BSE images, modeled coarse aggregate can be easily identified and removed. Due to the significant difference in hardness between granite and cement paste, the grinding and polishing process may cause a height difference between the two phases (Lyu et al. 2019). Along the aggregate and mortar interface, this appeared as a black narrow strip, which would be mistaken for pores or cracks by image analysis software according to the gray value, but it is the shadow produced by the height difference under the electron microscope (Lyu et al. 2019). Therefore, the shadow portion was removed together with the aggregate. The gray threshold recognition technique proposed by Wong et al. (2006) was adopted to distinguish pores and cracks, unreacted clinkers, and hydration products in ITZ and adjacent mortar matrix.

As shown in Figs. 4(b) and 5(b), there are two inflections in the cumulative gray curves of cement paste. Two intersections obtained by linear fitting on both sides can be used as the gray threshold for identifying constituents. Taking Fig. 4(b) as an example, gray values of 0–129, 129–139, and 139–254 represent pores and cracks,

hydration products, and unreacted clinkers, respectively. The 20 continuous strips with a width of  $5\ \mu\text{m}$  were taken out from the aggregate boundary to the mortar matrix. For ITZs with and without WGP, 30 BSE images were used to statistically analyze

the relationship between the volume fraction of each constituent and the distance from the aggregate boundary. The width of ITZs can be easily determined by image analysis results. The processing procedure of the BSE image is shown in Figs. 4 and 5.

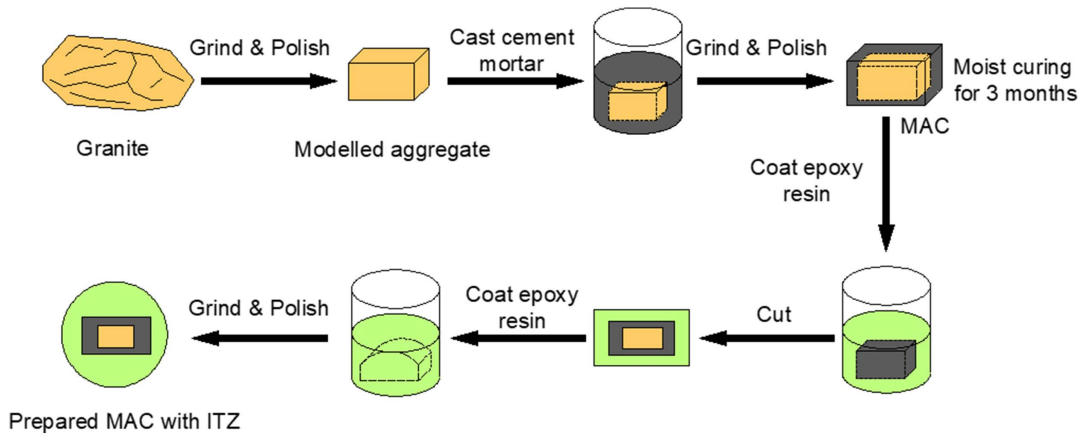


Fig. 3. Preparation process of ITZ simulated by MAC.

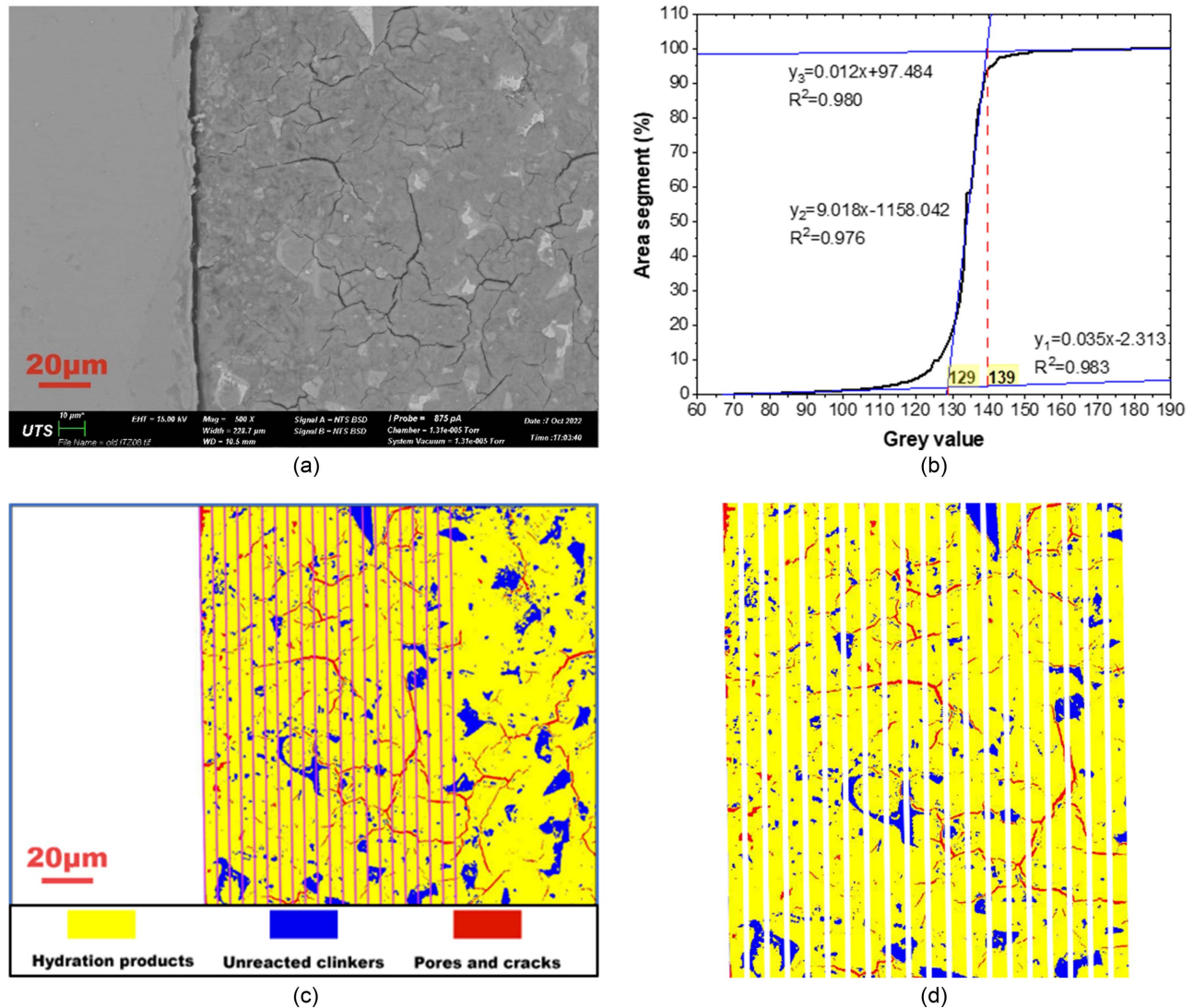
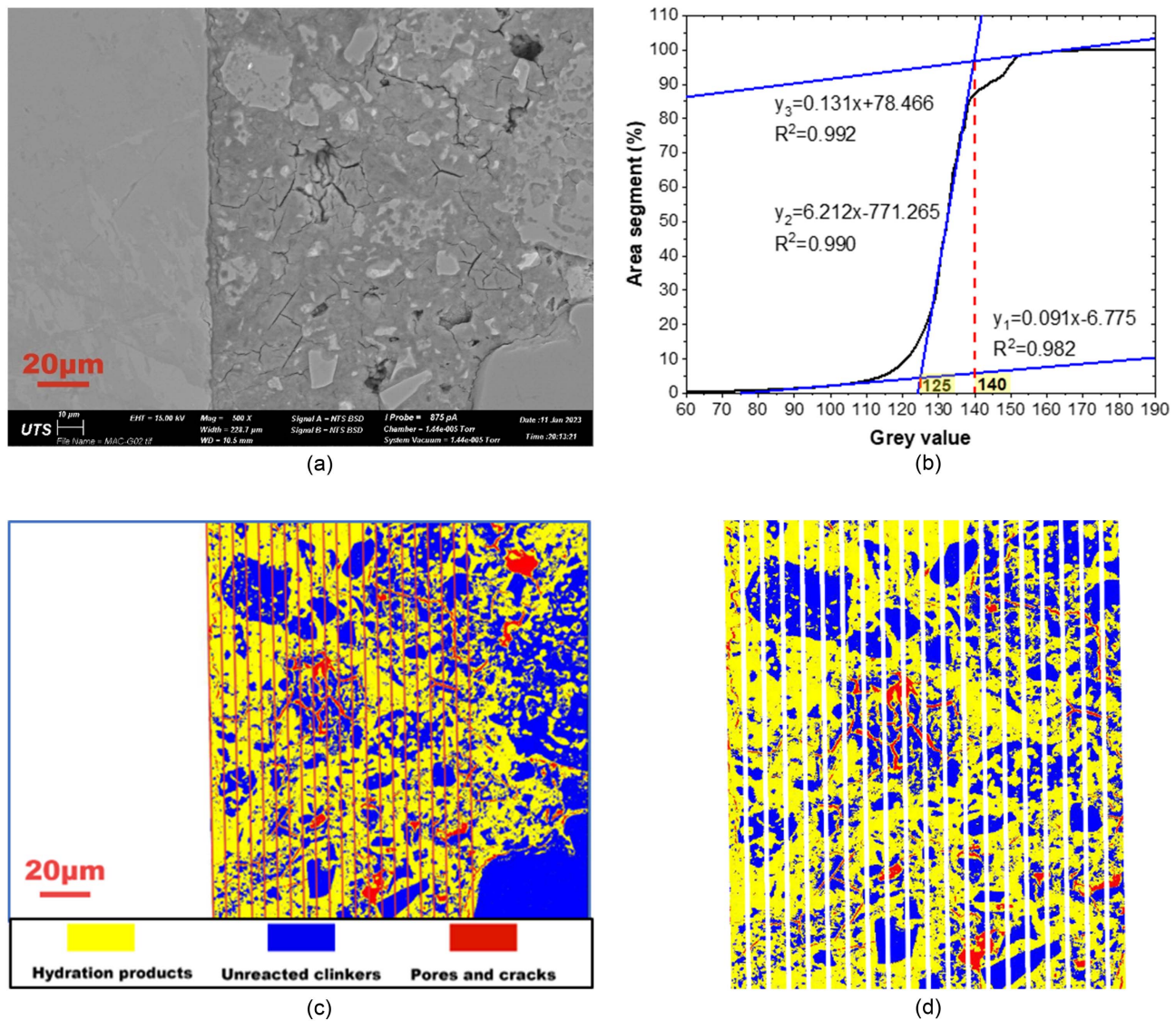


Fig. 4. BSE image processing procedure of ITZ without WGP: (a) BSE image of ITZ without WGP; (b) gray value threshold determination; (c) constituent segmentation; and (d) strip divisions.



**Fig. 5.** BSE image processing procedure of ITZ with WGP: (a) BSE image of ITZ with WGP; (b) gray value threshold determination; (c) constituent segmentation; and (d) strip divisions.

### Nanoindentation and Nanoscratch

The Agilent G200 Nano Indenter (Agilent Technologies, Santa Clara, California) can simultaneously apply normal and lateral forces to a sample. This enables the indenter to perform nanoindentation and nanoscratch tests simply by choosing the appropriate tip and testing method. The schematic diagram of nanoindentation and nanoscratch tests is shown in Fig. 6. When conducting nanoindentation tests, a Berkovich tip with a radius of 20 nm was installed. Grid nanoindentation combined with statistical analysis was used to reveal the micromechanical properties of the ITZ and its adjacent regions, which contributed to the understanding of the bond strength between aggregate and cement paste in concrete.

Concrete is a heterogeneous and multiphase structure. Although the sample surface was ground and polished during processing, it was still difficult to ensure that the region to be tested had perfect flatness. Therefore, the nanoindentation depth was made enough to avoid the negative influence of sample surface roughness. According to previous experience (Luo et al. 2021), the average depth was set to 800 nm to satisfy the test accuracy as well as the number of effective testing points within the ITZs. The loading force was

controlled by indentation depth. When the indentation depth was close to 800 nm, the load was maintained for 10 s to eliminate the influence of residual strain. After unloading to 10% of the peak load and maintaining for another 75 s, the indenter was completely detached from the sample surface.

Five regions avoiding large cracks and fine aggregate were selected for nanoindentation tests of ITZ of both with and without WGP specimens. For each nanoindentation region, as shown in Fig. 6,  $3 \times 5$  and  $11 \times 5$  measuring points were conducted on the granite block and cement paste, respectively. The vertical spacing of the measuring points was  $15 \mu\text{m}$ . The distance between the aggregate boundary and adjacent measuring points was  $4 \mu\text{m}$ . No measuring points were arranged on the aggregate boundary. The lateral spacing of the remaining measuring points was  $7 \mu\text{m}$ . According to previous research, the ITZ width in concrete is about  $15\text{--}50 \mu\text{m}$  (Scrivener et al. 2004; Diamond and Huang 2001). Therefore, the designed grid nanoindentation area can cover the ITZ and a part of the adjacent matrix. The following image analysis technique will be used to identify the ITZ width of the samples in this study and confirm this inference.

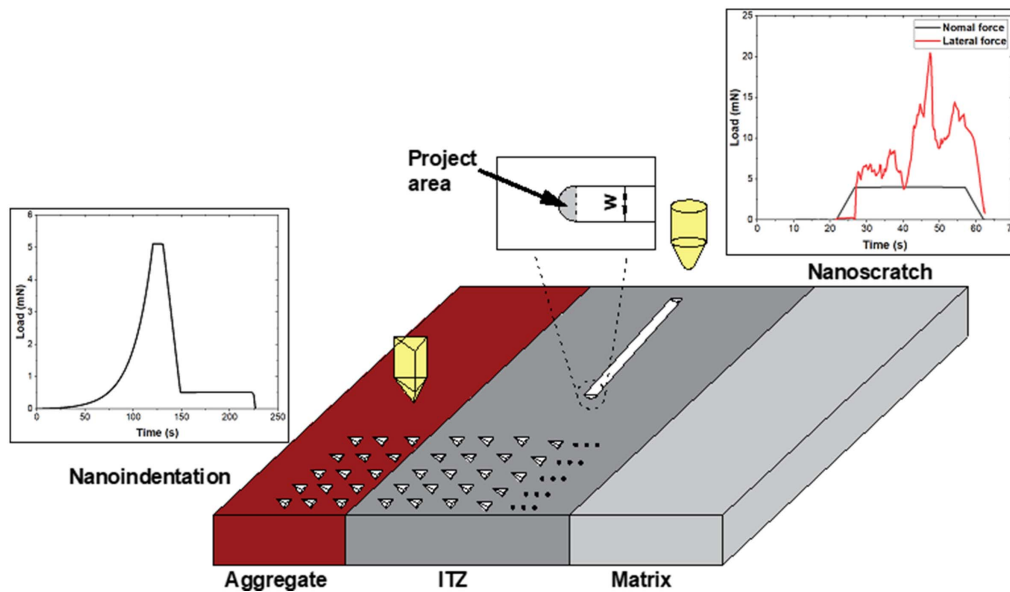


Fig. 6. Schematic diagram of nanoindentation and nanoscratch.

Finally, the elastic modulus and hardness within ITZ at different distances from the aggregate boundary can be obtained by load-indentation depth curve, characteristics of the tip, characteristics of the sample, and projected contact area ( $A$ ) according to Eqs. (1)–(3)

$$H = \frac{P_{\max}}{A} \quad (1)$$

$$S = \frac{dP}{dh} \Big|_{h=h_{\max}} = \frac{2}{\sqrt{\pi}} E_r \sqrt{A} \quad (2)$$

$$\frac{1}{E_r} = \frac{1-v^2}{E} + \frac{1-v_i^2}{E_i} \quad (3)$$

where  $P$  = indentation load;  $h$  = indentation depth;  $E_r$  = reduced elastic modulus;  $E_i$  = elastic modulus;  $v_i$  = Poisson's ratio of the tip;  $E$  = elastic modulus;  $v$  = Poisson's ratio of the sample; and  $A$  = projected contact area.

For nanoscratch tests, a hemispherical tip with a radius ( $r$ ) of  $5 \mu\text{m}$  and apex angle ( $\alpha$ ) of  $60^\circ$  was adopted to avoid the errors caused by the asymmetry of the Berkovich tip on the test results. Different from nanoindentation, nanoscratch depth ( $d$ ) was controlled by the normal force. The maximum normal force ( $F_{N\max}$ ), scratch speed ( $v_s$ ), and scratch distance ( $L$ ) can be defined by the test method according to standards [ASTM G171-03 (ASTM 2005)] and previous research results (Li et al. 2021; Luo et al. 2022). A moderate maximum normal force can ensure relatively accurate test results while avoiding the interference of aggregate constraints (Li et al. 2021; Luo et al. 2022).

In this study, the normal force was uniformly increased to 4 mN during the prescratch process, and then, the normal force was kept at peak value and  $4 \mu\text{m/s}$  of scratch speed until the scratch distance obtained 120  $\mu\text{m}$ . Finally, the loading procedure entered the post-scratch stage until the tip left the sample surface. The data acquisition rate was set to 1 point/ $\mu\text{m}$ .

A total of 20 scratches were randomly conducted along the center of the ITZ and the matrix 30  $\mu\text{m}$  away from the ITZ, respectively. Regions close to fine aggregate and large cracks were

artificially avoided. The scratch hardness ( $HS_p$ ) and fracture toughness ( $K_c$ ) of samples were calculated based on Eqs. (4)–(7). The geometric depth ( $d_{gt}$ ) and the corresponding scratch width ( $w_{gt}$ ) were 2,500 nm and 5  $\mu\text{m}$ , respectively. The transverse force ( $F_T$ ) was obtained directly from the test results

$$HS_p = \frac{8F_{N\max}}{\pi w^2} \quad (4)$$

$$K_c = \frac{2\sqrt{2}F_T}{\pi\sqrt{w^3}} \quad (5)$$

$$w = \begin{cases} 2\sqrt{r^2 - (r-d)^2}d \leq d_{gt} \\ w_{gt} + 2 \tan\left(\frac{\alpha}{2}\right) \times (d - d_{gt})d > d_{gt} \end{cases} \quad (6)$$

$$d_{gt} = r \left( 1 - \sin\left(\frac{\alpha}{2}\right) \right) \quad (7)$$

### Chemical and Mineralogical Composition

EDS mapping analysis was used to observe the chemical elements distribution within ITZs and the adjacent regions under the background of BSE images with a magnification of 1,500 $\times$ . During the EDS test, the accelerating voltage and working distance remained at 15 kV and 10 mm, and the probe current was lower than that of the BSE to reduce dead time to a reasonable level. The distributions of Al, Si, Ca, and Na were observed. In addition, the atomic ratio of Si/Ca versus Si/Na was stoichiometrically quantified by a peak to the background with self-calibrating methods (P/B-ZAF).

XRD patterns of cement mortar with and without WGP were obtained by a Bruker D8 Discover diffractometer (Bruker Corporation, Berlin). The mineralogical characterizations of the two groups of samples were analyzed at a range of  $5^\circ$ – $70^\circ 2\theta$ , with a  $0.02^\circ$  step.  $\text{CuK}\alpha$  radiation of wavelength 1.54  $\text{\AA}$  was applied to measure diffraction patterns. FTIR spectra of samples with and without WGP were obtained by a Nicolet 6,700 FTIR spectrometer (Thermo Fisher Scientific, Waltham, Massachusetts). The wave number ranged from 4,000 to 500  $\text{cm}^{-1}$ , and a resolution of 8  $\text{cm}^{-1}$

was adopted to analyze the contents of portlandite, ettringite, C-S-H gel, and others through chemical bonds.

## Results and Discussions

### Constituent Distribution within ITZs

The statistical results of image analysis are shown in Fig. 7. The proportion of hydration products was directly related to unreacted clinkers. That is, when the content of hydration products increased with the distance from the aggregate boundary, the proportion of unreacted particles decreased, and vice versa. The proportion of pores and cracks was the highest near the aggregate boundary and decreased rapidly to a stable value with distance from the modeled aggregate. Due to the wall effect on the distribution of clinkers and free water in concrete, the width of ITZ can be determined by the region where the proportion of hydration products and unreacted clinkers changed most significantly (Fang and Zhang 2020). Therefore, the ITZ widths of the modeled samples with and without WGP were approximately 10 and 30  $\mu\text{m}$ , respectively. The ITZ and matrix in Fig. 7 were separated by dashed lines. The average proportions and corresponding standard deviations of phases in ITZs and the adjacent matrix are listed in Table 2.

It can be roughly seen from the phase segmentation image in Figs. 4 and 5 that the content of unreacted clinkers in the sample with WGP was higher than that in the counterpart, and the particle size gradually increased with the distance from the boundary of the granite block. In fact, the statistical results in Table 2 indicate that the ITZ containing WGP possessed a lower proportion of unreacted clinkers and a higher proportion of hydration products compared with the ITZ without WGP, whereas the trends were opposite

for the matrix, and the data dispersion of samples with WGP was larger. This is attributed to the nucleation effect of WGP, which offers additional space and nucleation sites for cement particles to hydrate (Hjorth et al. 1988; Lothenbach et al. 2011; Mahmood et al. 2022). A similar phenomenon was also found in the analysis of the distribution of fly ash and slag clinkers in geopolymer concrete (Luo et al. 2022; Fang and Zhang 2020). For example, Fang and Zhang (2020) found that the diameter of grains distributed in ITZ was much smaller than that in the mortar matrix.

For pores and cracks, the proportion in the ITZ with WGP was slightly higher than that in the sample without WGP, whereas the proportion in the matrix with WGP was significantly reduced. Part of WGP participated in the pozzolanic reaction to generate more C-S-H gels and filled gaps (Nassar and Soroushian 2012). In addition, the rough and angular surface of WGP provided a site for C-S-H nucleation reactions, which promoted cement hydration, and the rest of the unreacted WGP can also play the role of filler to improve the pore structure (Mirzahosseini and Riding 2015; Du and Tan 2017).

### Elements and Mineralogical Composition of ITZs

#### EDS Analysis

GP cement and soda-lime glass powder were the main cementitious materials in this study. A BSE image was used as background, and the distributions of Al, Si, Ca, and Na are shown in Fig. 8 by EDS mapping. The region with a relatively uniform distribution of Si and Ca was C-S-H gel. It can be understood that cement hydration in MAC with and without WGP has reached a high level. There were more Al-rich regions in the ITZ without WGP, whereas more Si- and Na-rich regions appeared in the ITZ with WGP. This is because in the sample containing WGP, there was less cement,

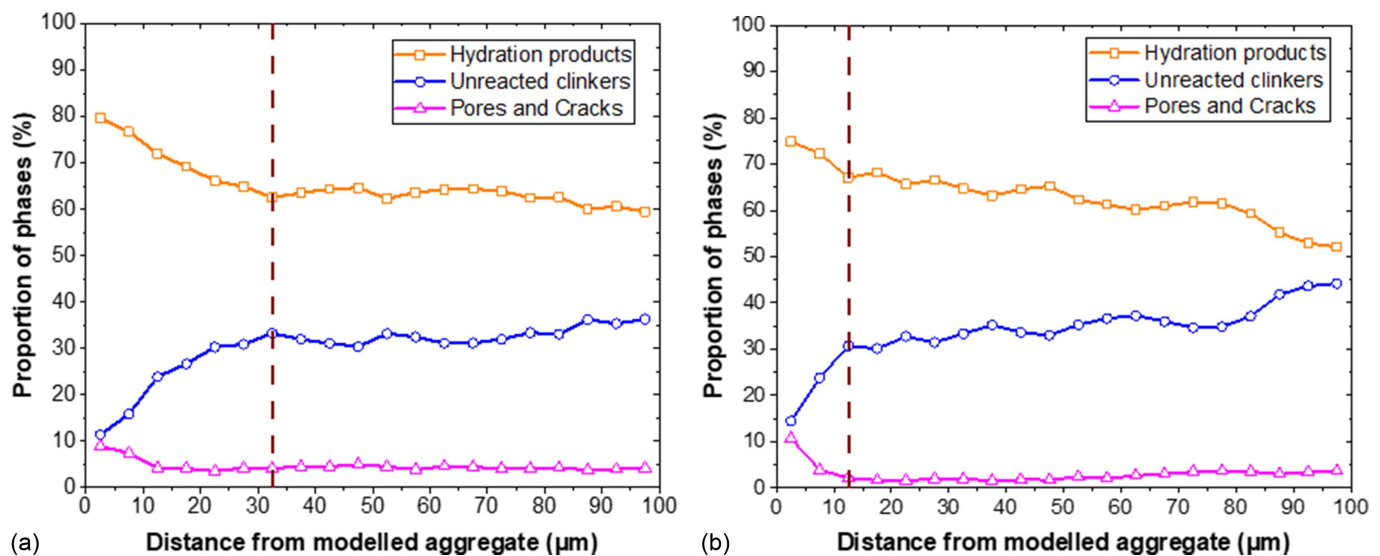
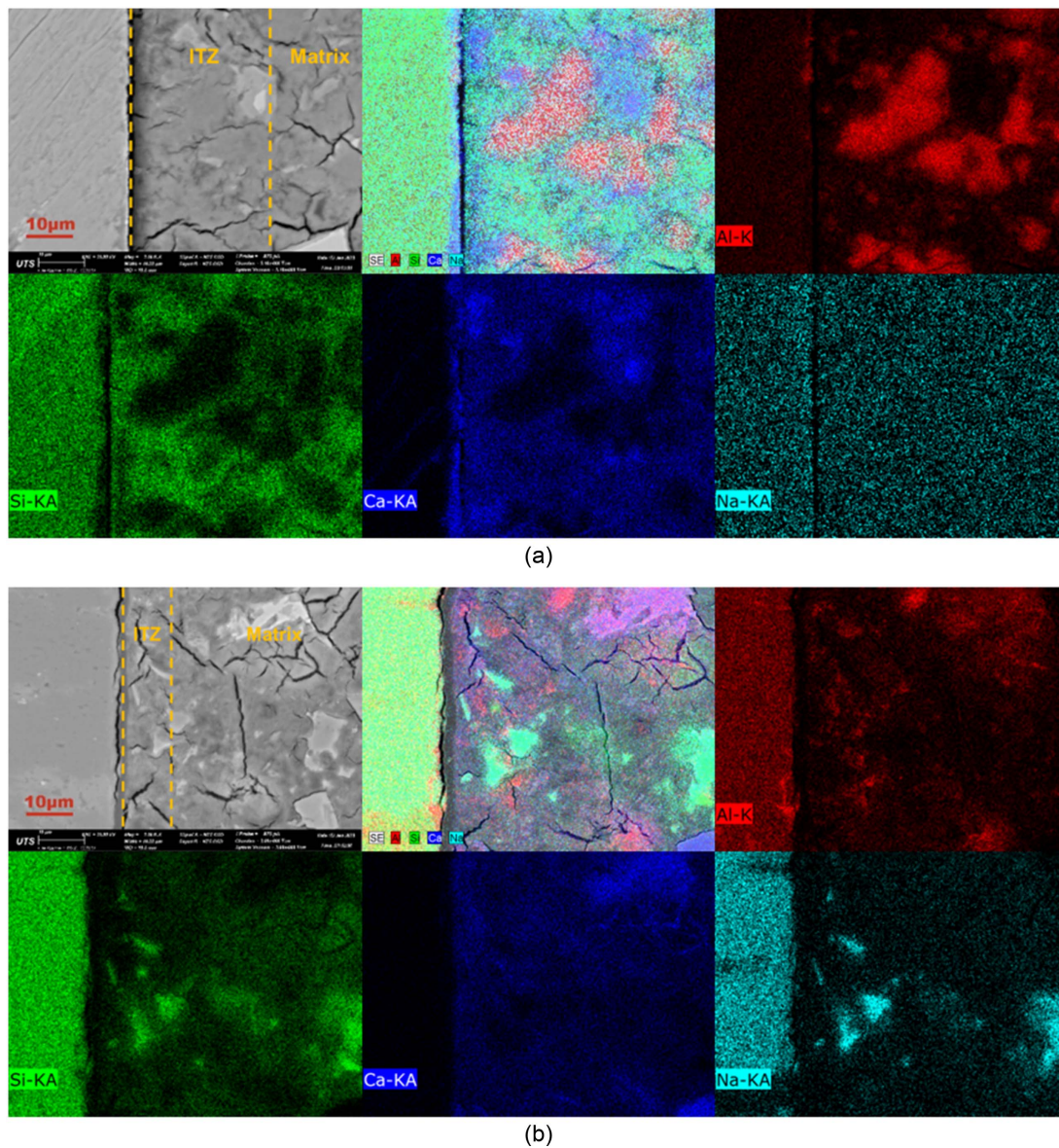


Fig. 7. Phase distributions in ITZs and adjacent mortar matrix: (a) modeled sample without WGP; and (b) modeled sample with WGP.

Table 2. Average proportion of different phases in image analysis

| Sample ID | Hydration products (%) |               | Unreacted clinkers (%) |               | Pores and cracks (%) |               |
|-----------|------------------------|---------------|------------------------|---------------|----------------------|---------------|
|           | ITZ                    | Mortar matrix | ITZ                    | Mortar matrix | ITZ                  | Mortar matrix |
| MAC-C     | 70.16 ± 5.84           | 62.80 ± 1.68  | 24.61 ± 7.58           | 32.89 ± 1.89  | 5.23 ± 1.92          | 4.31 ± 0.32   |
| MAC-G     | 71.45 ± 3.23           | 61.52 ± 4.44  | 22.99 ± 6.68           | 35.94 ± 3.87  | 5.56 ± 3.68          | 2.54 ± 0.79   |



**Fig. 8.** EDS mapping analysis of ITZs and adjacent matrix: (a) chemical elements distribution of ITZ without WGP; and (b) chemical elements distribution of ITZ with WGP.

but a good amount of partially reacted WGP containing higher concentrations of  $\text{SiO}_2$  and  $\text{Na}_2\text{O}$  remained within the ITZ.

Fig. 9 depicts the quantitative analysis results based on EDS mapping in random regions of ITZ and matrix. The data cluster area represented C-S-H gel, except some data with Si/Ca and Si/Na close to zero may refer to pores and cracks. The Si/Ca of C-S-H in the ITZ and matrix without WGP was mainly concentrated around 0.5, whereas WGP generated more C-S-H gels with Si/Ca in the range of 1–2. It has been known that C-S-H with high Si/Ca had higher cohesion strength (Kunther et al. 2017). Combining the proportion of hydration products in Table 2, it can be reasonably speculated that ITZ exhibited higher performance in samples containing WGP.

In addition, the dot where the Si/Ca ratio was close to 7 represents WGP according to the oxide components listed in Table 1. As expected, after adding 20% WGP, the number of these dots significantly increased in the ITZ and matrix. However, the existing data with a high Si/Ca ratio in ITZ and matrix without WGP may be due to the interference of silica sand in the samples. Although

locations for EDS point mapping were carefully chosen to avoid sand grains in the microstructure, a few might have interfered resulting in outliers with high Si/Ca ratios. In addition, the Si/Na ratio of the ITZ and matrix were lower in the sample with WGP because the cement was replaced by high-Na glass powder.

#### XRD Analysis

Specific crystals exposure to a beam of incident X-rays can cause diffraction in specific directions. Comparing the diffraction intensities in different directions with the standard powder diffraction data can determine the crystal phases in the material (Qu et al. 2022). The mortar part of MAC with and without WGP was cut and ground into powder for XRD testing, and the corresponding XRD patterns are shown in Fig. 10. Because the powder sample contained silica sand, there were many more quartz diffraction peaks in the XRD patterns than previous research on paste samples (Lu et al. 2020; Du and Tan 2017). The diffraction peaks corresponding to portlandite appeared at around  $18.09^\circ 2\theta$ ,  $34.14^\circ 2\theta$ ,  $47.16^\circ 2\theta$ , and  $50.82^\circ 2\theta$ . Comparing the XRD spectra, the content

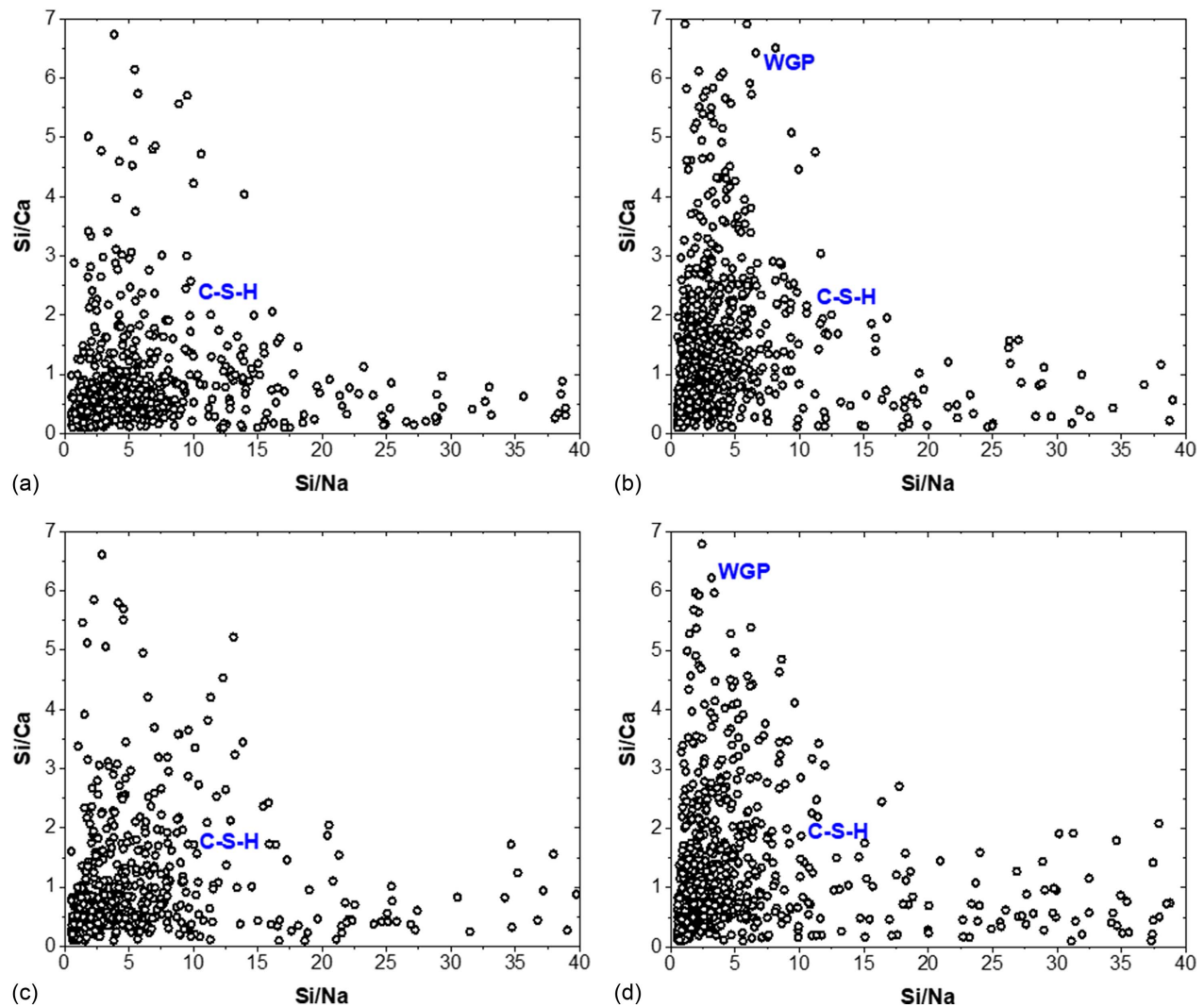


**Fig. 9.** Statistical analysis results of EDS mapping: (a) ITZ without WGP; (b) ITZ with WGP; (c) mortar matrix without WGP; and (d) mortar matrix with WGP.

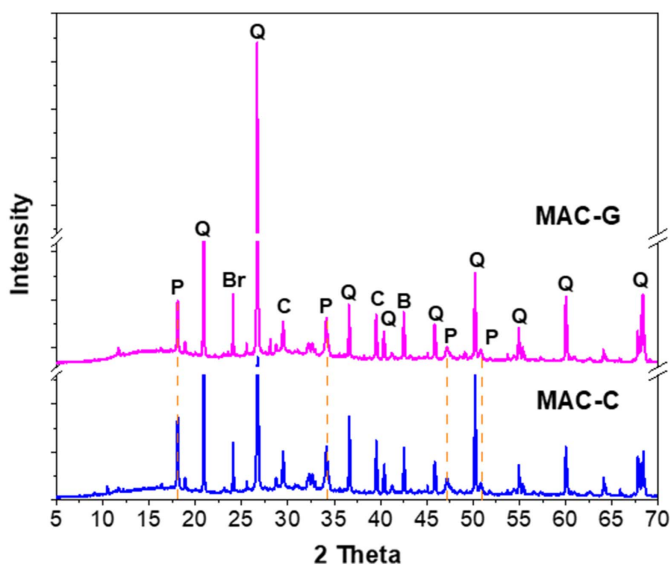


**Fig. 10.** XRD patterns of cement mortar with (MAC-G) and without (MAC-C) WGP at age of 3 months. Q = quartz; P = portlandite; B = belite; Br = brownmillerite; and C = calcite.

of portlandite in the sample decreased when 20% of cement was substituted by WGP. It should be admitted that the cement dilution reduced the peak density of portlandite. According to the change of Si/Ca ratio in Fig. 9 and previous research results (Omran and Tagnit-Hamou 2016; Ismail and Al-Hashmi 2009), the reaction of amorphous silica in WGP with  $\text{Ca}(\text{OH})_2$  to generate C-S-H was another important reason leading to the decrease of portlandite peaks.

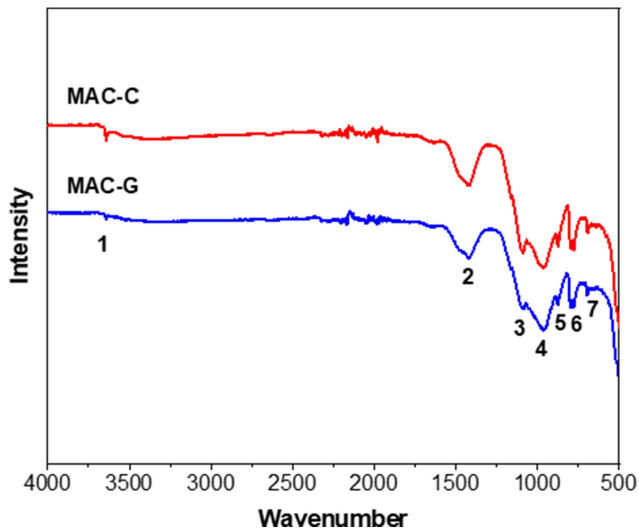
#### FTIR Analysis

Fig. 11 shows the FTIR spectrum of samples with and without WGP in this study. Band 1 at around  $3,642\text{ cm}^{-1}$ , typical of the O-H stretching vibrations generated by portlandite ( $\text{Ca}(\text{OH})_2$ ) (Garcia-Lodeiro et al. 2009; Lu et al. 2022), indicates that WGP consumed a certain amount of portlandite to generate C-S-H gel. This is consistent with the aforementioned XRD analysis results and the conclusions observed by other researchers through SEM and TGA (Mirzahosseini and Riding 2015; Mostofinejad et al. 2020; Ye et al. 2022). The remaining bands were mainly concentrated between  $1,500$  and  $500\text{ cm}^{-1}$ , and the corresponding band assignments are listed in Table 3.

To compare the content of components in samples, the FTIR spectra between  $1,300$  and  $700\text{ cm}^{-1}$  were separated into four

independent peaks at around 785, 869, 975, and 1,100  $\text{cm}^{-1}$ , with a shoulder at 1,180  $\text{cm}^{-1}$  by Gaussian mixture models (Fig. 12).

The frequency values of the peaks and respective area fractions obtained from statistical deconvolution are given in Table 4. The peaks at around 785 and 975  $\text{cm}^{-1}$  were characteristic of the stretching vibrations generated by Si-O bonds in  $Q^1$  and  $Q^2$  (C-S-H),



**Fig. 11.** FTIR spectra of cement mortar with (MAC-G) and without (MAC-C) WGP at the age of 3 months.

**Table 3.** Sample powder with and without WGP assignments

| Band | Frequency ( $\text{cm}^{-1}$ ) | Assignment                            |
|------|--------------------------------|---------------------------------------|
| 1    | 3,642                          | $\nu$ OH [ $\text{Ca}(\text{OH})_2$ ] |
| 2    | 1,420                          | $\nu_3$ CO ( $\text{CO}_3^{2-}$ )     |
| 3    | 1,090                          | $\nu$ Si-O                            |
| 4    | 965                            | $\nu$ Si-O (C-S-H) $Q^2$              |
| 5    | 874                            | $\nu_2$ CO ( $\text{CO}_3^{2-}$ )     |
| 6    | 797                            | $\nu$ Si-O (C-S-H) $Q^1$              |
| 7    | 693                            | $\nu_2$ CO ( $\text{CO}_3^{2-}$ )     |

respectively (Garcia-Lodeiro et al. 2008). The area fractions of  $Q^1$  and  $Q^2$  in the cement mortar with WGP increased by 2.06% and 4.19%, respectively, compared with the sample without WGP, indicating that more C-S-H gel was generated after adding WGP. In addition, the  $Q^2$  peak tended to shift toward higher frequencies with the improvement of the Si/Ca ratio due to the progressive depolymerization of the silicate chain (Garcia-Lodeiro et al. 2009). The frequency shifted from 974 to 980  $\text{cm}^{-1}$  when 20% WGP was added to the sample, representing that more C-S-H with a high Si/Ca ratio was generated (Garcia-Lodeiro et al. 2009), which corresponds to the results in Fig. 9.

The appearance of the peak at frequencies around 1,180  $\text{cm}^{-1}$  is attributed to silica-rich gel (Garcia-Lodeiro et al. 2009). The signal of this peak was stronger in the sample with WGP, suggesting a more condensed microstructure. The peaks at around 869 and 1,100  $\text{cm}^{-1}$  corresponded to C-O( $\text{CO}_3^{2-}$ ) and S-O (mainly for ettringite), respectively (Garcia-Lodeiro et al. 2008). The data in Table 4 indicate that the area fraction of the peak corresponding to C-O increased by 0.29% in the sample containing WGP, whereas the figure corresponding to S-O decreased by 7.3% compared with the counterpart.

The generation of ettringite and carbonation of cement paste were largely controlled by the content of soluble alkali metal oxides (mainly CaO and  $\text{Na}_2\text{O}$ ) (Qu et al. 2021). A high concentration of  $\text{Na}_2\text{O}$  could increase the pH value of the pore solution. The alkali environment accelerated the carbonization speed of cement paste and enhance the solubility of ettringite (Qu et al. 2021). Moreover, ettringite was formed by combining CaO with  $\text{Al}^{2+}$  and  $\text{SO}_4^{2-}$  (Li et al. 2020). WGP contained more  $\text{Na}_2\text{O}$  than CaO in Table 1.

**Table 4.** Results obtained from the statistical deconvolution of FTIR spectra from 1,300 to 700  $\text{cm}^{-1}$

| MAC-C                          |          | MAC-G                          |          |
|--------------------------------|----------|--------------------------------|----------|
| Frequency ( $\text{cm}^{-1}$ ) | Area (%) | Frequency ( $\text{cm}^{-1}$ ) | Area (%) |
| 1,181                          | 1.82     | 1,175                          | 3.88     |
| 1,100                          | 33.79    | 1,104                          | 26.49    |
| 974                            | 54.68    | 980                            | 58.87    |
| 869                            | 3.30     | 869                            | 3.59     |
| 785                            | 6.40     | 785                            | 7.16     |

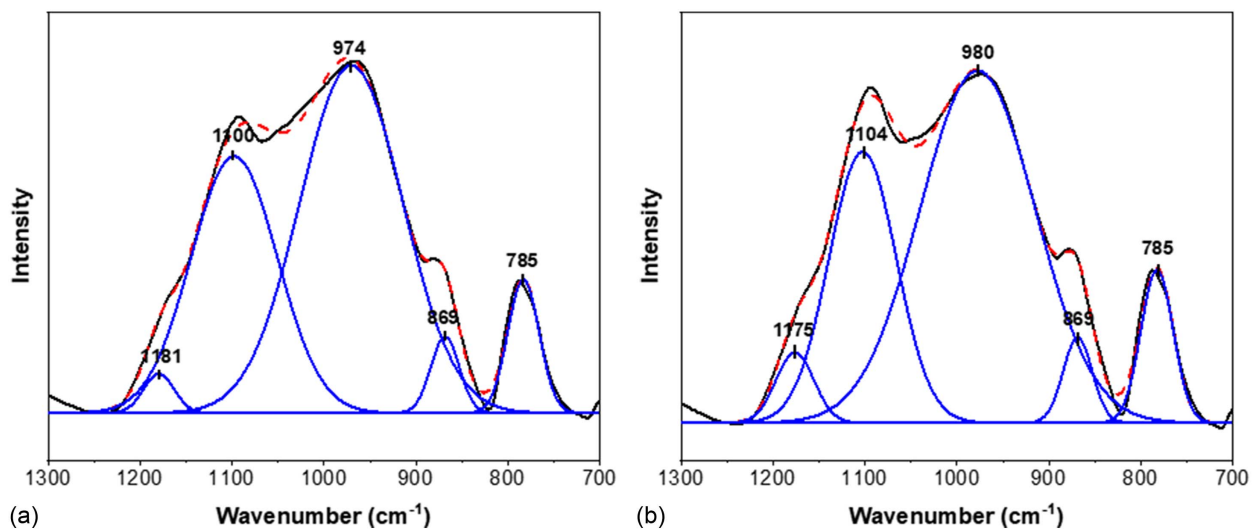


**Fig. 12.** Deconvolution spectra of mixtures from 700 to 1,300  $\text{cm}^{-1}$ .

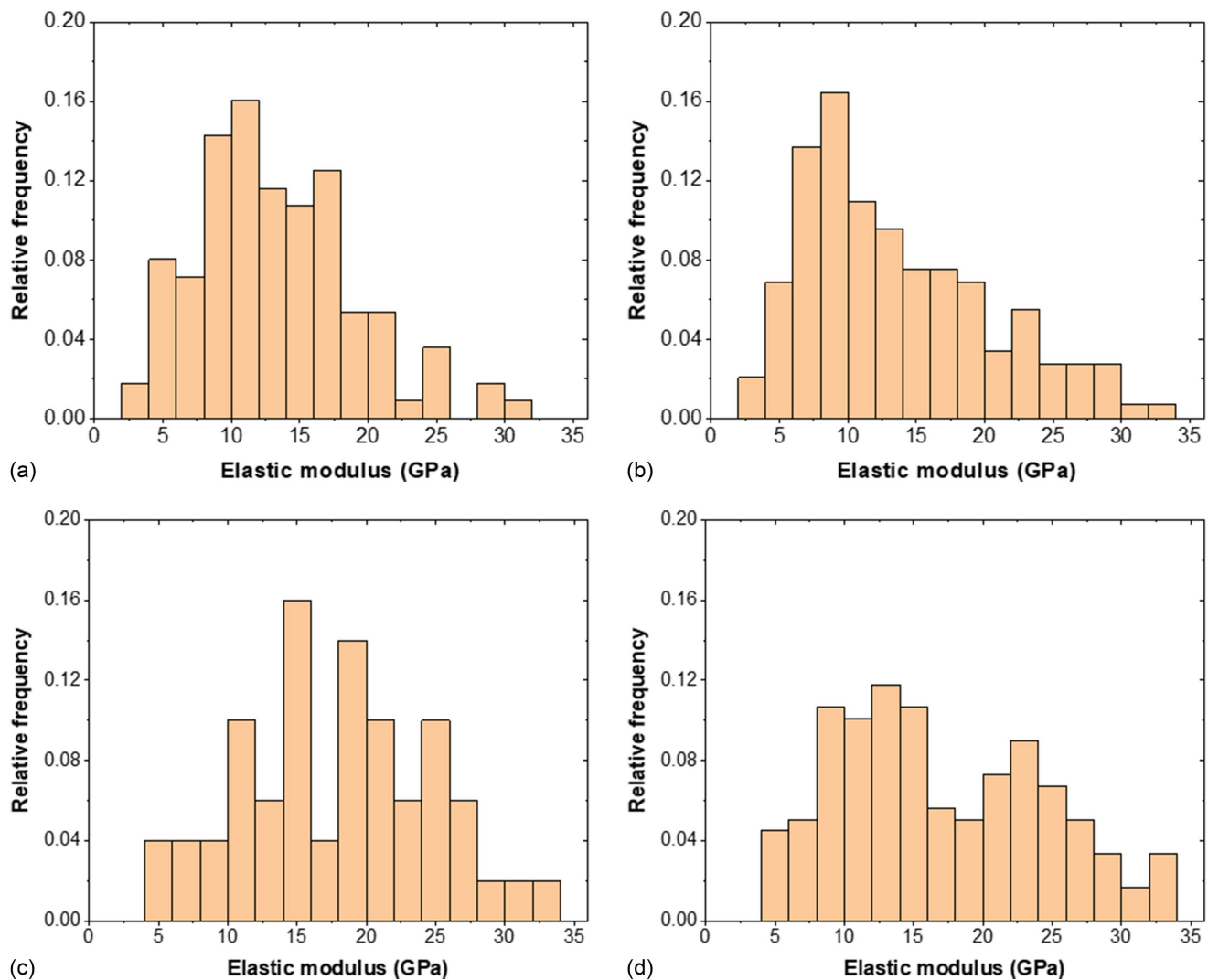


**Fig. 13.** Elastic modulus statistical results obtained from nanoindentation tests (bin size = 2 GPa): (a) ITZ without WGP; (b) mortar matrix without WGP; (c) ITZ with WGP; and (d) mortar matrix with WGP.

As a result, compared with the sample without WGP, the peak corresponding to C-O was strengthened after adding WGP, whereas the peak corresponding to S-O weakened.

### Nano- and Micromechanical Properties of ITZs

#### Nanoindentation Test Results

The elastic modulus of materials can be determined from the slope of the load versus indentation depth unloading curve. The frequency density distribution histograms (FDH) of elastic modulus for ITZ and the adjacent matrix for specimens with and without WGP are shown in Fig. 13. The results show that the elastic modulus of ITZ and matrix of MAC without WGP followed an approximately normal distribution. For ITZ and adjacent matrix without WGP in Figs. 13(a and b), the elastic modulus with a relative frequency higher than 0.04 were distributed in the ranges of 5–20 and 5–23 GPa, respectively. The weighted mean elastic modulus was 13.29 and 13.64 GPa, respectively, which is in line with the traditional concept of the micromechanical difference between ITZ and matrix in cement-based materials (Luo et al. 2018, 2019).

However, some recent studies reported an opposite conclusion (Luo et al. 2021; Diamond and Huang 2001). There was more CH

in the ITZ, resulting in a slightly higher measured elastic modulus of the ITZ than that of the mortar matrix (Luo et al. 2021). However, the test results still approved the conclusion that the ITZ was the weakest part of concrete because the cohesiveness of CH can be neglected (Luo et al. 2021).

The curing age of the MAC samples in this study was more than 3 months. Combined with the EDS mapping analysis in Fig. 8(a), there was almost no obvious  $\text{Ca}^{2+}$ -rich area within ITZ, indicating that the cement hydration has reached a relatively high level (Kunther et al. 2016). Most of the nanoindentation data in Figs. 13(a and b) can be regarded as the mechanical properties of gel products. As a result, it can be inferred that the cohesion of C-S-H in the mortar matrix was greater than that in ITZ without WGP, which explains why cement composites are prone to fail along the ITZ; better cohesion imparts better mechanical properties (compressive strength, flexural strength, tensile strength, and elastic modulus, and so on).

It is worth noting that the elastic modulus of ITZ and matrix with WGP was distributed over a wider range, and two remarkable peaks appeared. The first peak ranged from 10 to 15 GPa, mainly reflecting the mechanical properties of the C-S-H gel. According to the literature, the elastic modulus of cement paste was generally between 10 and 20 GPa, whereas the elastic modulus of glass

particles can be as high as 80 GPa (Khedmati et al. 2018, 2019; del Bosque et al. 2017). The second peaks at 19–27 GPa in Figs. 13(c and d) could represent the mixed phase of gel and partially reacted glass particles. It can also be concluded that the heterogeneity of ITZ and matrix with WGP was more significant.

### Nanoscratch Results

Nanoscratch can provide far more test data than nanoindentation in a short operation time. The huge amount of data made it possible to use a very small bin size for frequency density statistical analysis, revealing more phases but not disordering the shape of the histogram (Li et al. 2021). After trial and error, the bin size was finally determined to be 0.05 GPa. However, the tip radius and the displacement into the surface of the nanoscratch were usually higher than those of nanoindentation, which led to a higher project area than nanoindentation tests. As a result, the nanoscratch results often reflect the mixed results of multiple phases. Nevertheless, most of the test values can still represent the micromechanical properties of C-S-H due to the deliberate avoidance of large pores and aggregate in the test.

Fig. 14 shows the FDH of fracture toughness of ITZ and matrix with and without WGP obtained from nanoscratch tests. Fracture toughness quantitatively evaluates the ability of a material with

natural defects to resist rapid and unlimited crack propagation (Yan et al. 2022). The FDH of fracture toughness of ITZ without WGP can be separated into two components by the Gaussian mixture model. The expected values of fracture toughness for these two components were 0.18 and 0.39  $\text{MPa} \cdot \text{m}^{1/2}$ , which could be regarded as low-density C-S-H and high-density C-S-H, respectively. In contrast, there was only one independent peak in the mortar matrix without WGP. The expected value of fracture toughness of this component was 0.40  $\text{MPa} \cdot \text{m}^{1/2}$ , indicating that the gel phase in the matrix without WGP was mainly composed of high-density C-S-H with better homogeneity and cohesion strength, compared with the weaker C-S-H gel structure in the ITZ.

For ITZ and mortar matrix with WGP, the FDH of fracture toughness can be segmented into an independent peak with a shoulder. It can be seen from deconvolution analysis that the standard deviation of fracture toughness of ITZ and matrix with WGP was higher than their counterparts, indicated by shorter and wider distribution curves. The expected value of the peak was around 0.37  $\text{MPa} \cdot \text{m}^{1/2}$ . It can be explained that the WGP promoted the formation of C-S-H with a high Si/Ca ratio, improving the density of the ITZ and matrix, that is, the sample containing 20% WGP had more high-density C-S-H. The explanation of the shoulder with the

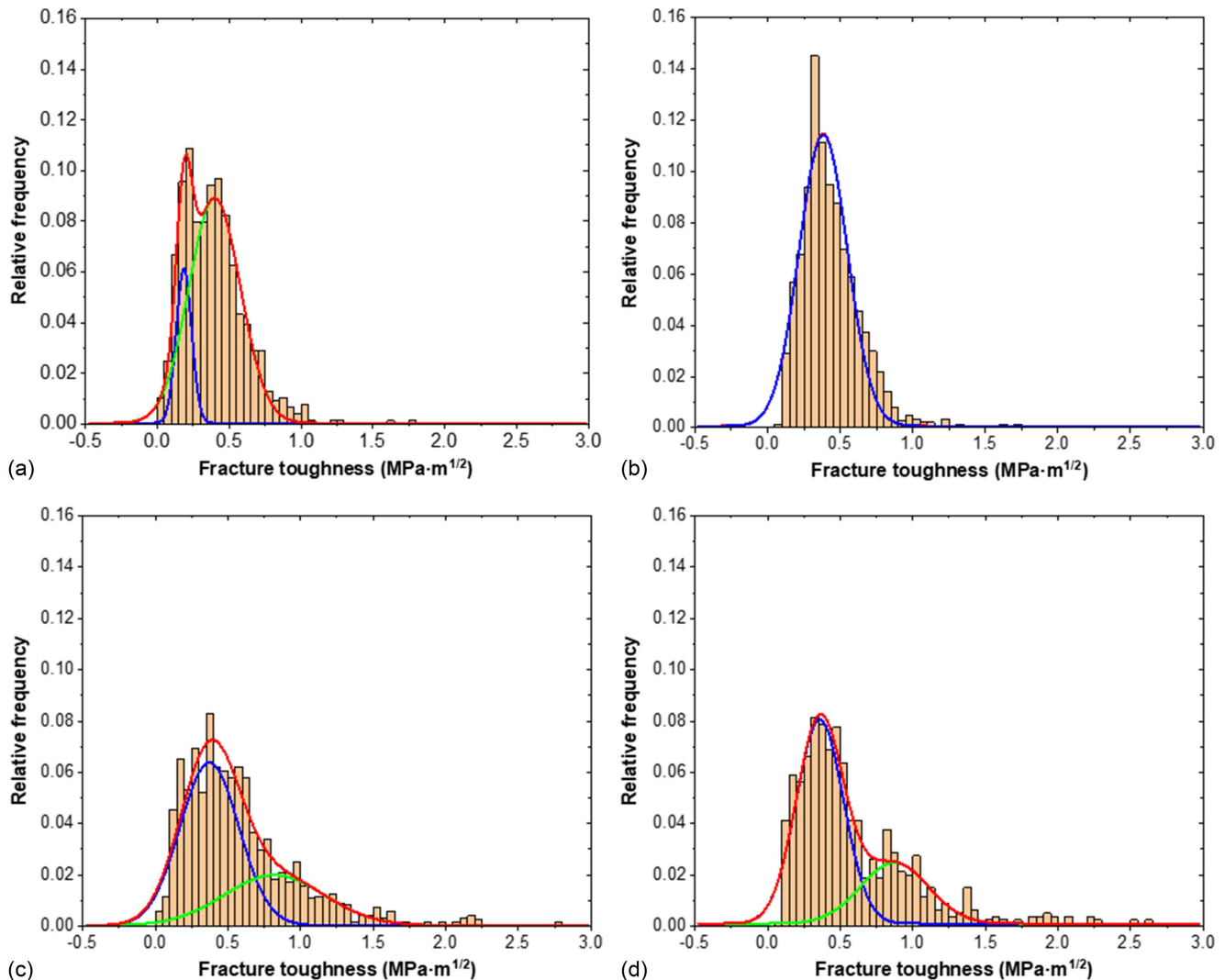


**Fig. 14.** Fracture toughness statistical results and deconvolution analysis obtained from nanoscratch (bin size=0.05 GPa): (a) ITZ without WGP; (b) mortar matrix without WGP; (c) ITZ with WGP; and (d) mortar matrix with WGP.

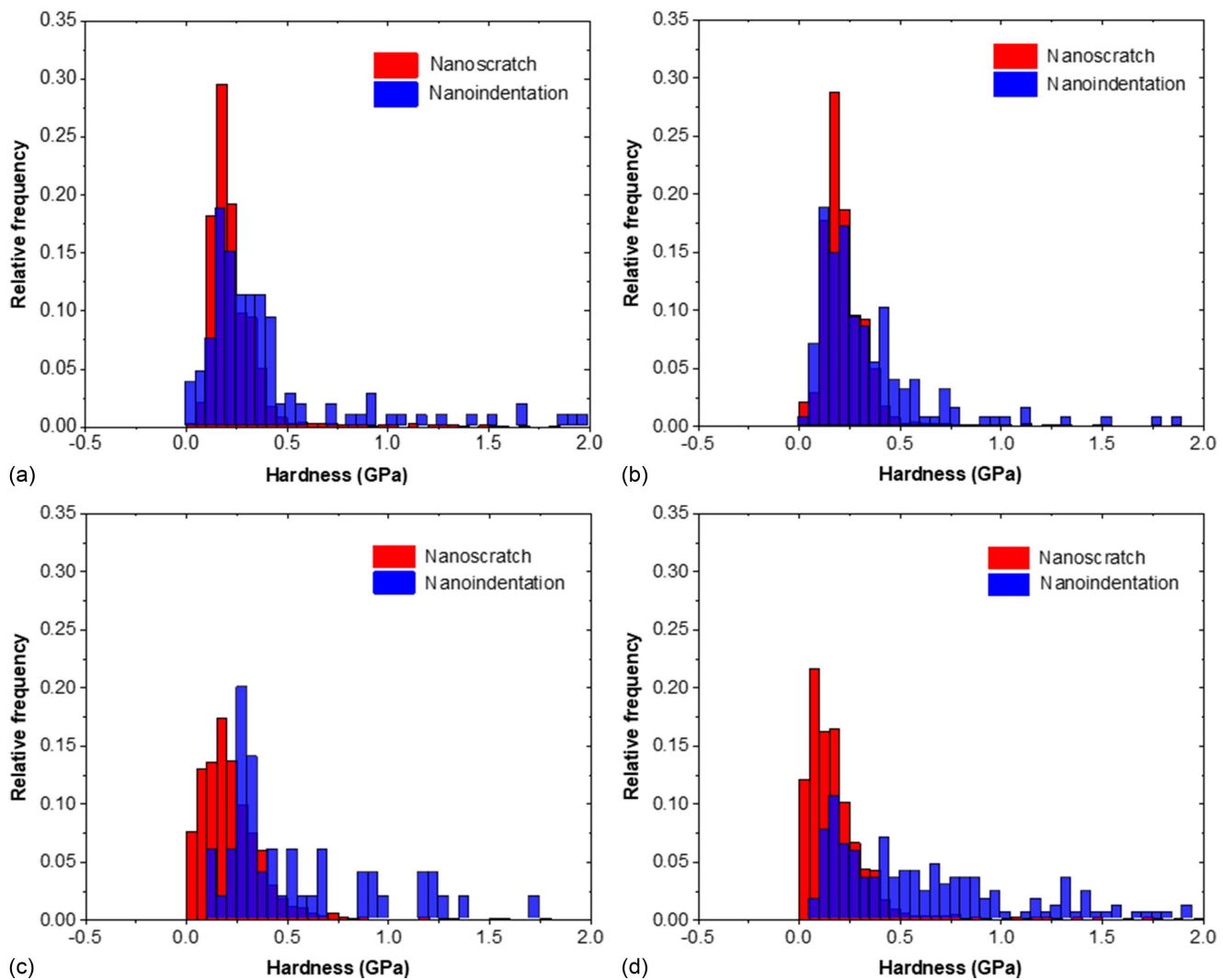


**Fig. 15.** Comparison of nanoindentation and nanoscratch results (bin size = 0.05 GPa): (a) ITZ without WGP; (b) mortar matrix without WGP; (c) ITZ with WGP; and (d) mortar matrix with WGP.

expected value of  $0.86 \text{ MPa} \cdot \text{m}^{1/2}$  can refer to the second peak in Figs. 13(c and d), which is the mixed phase of C-S-H and incompletely reacted WGP.

#### Comparison of Nanoindentation and Nanoscratch Results

Fig. 15 compares the nanoscratch hardness and nanoindentation hardness of samples with and without WGP. Because of the huge amount of data, the nanoscratch hardness of samples still followed an approximate normal distribution even if a very small bin size was adopted in histograms. In contrast, the nanoindentation hardness data were more discrete, and there were gaps between some values. Nevertheless, for samples without WGP, the main data of nanoindentation hardness and nanoscratch hardness can still achieve good concordance. By observing Figs. 15(a and b), it can be reasonably identified that the hardness of ITZ and matrix without WGP ranged from 0.125 to 0.375 GPa. In comparison, when 20% WGP was added to the sample, the hardness of ITZ and matrix was distributed in a wider range, which is similar to elastic modulus in Fig. 13 and fracture toughness in Fig. 14.

In the test results of nanoscratch, the value of the first two bars of the sample with WGP was higher than that of the sample without WGP. This is due to the presence of softer C-S-H gel within the sample containing WGP although the microstructure was denser,

and the unreasonable data corresponding to the large pores and cracks in the ITZ and matrix without WGP were removed in the statistical analysis. Therefore, there were more low-hardness constituents ( $\leq 0.1 \text{ GPa}$ ) in the nanoscratch test results of ITZ and matrix with WGP. It is worth noting that the nanoindentation hardness of ITZ and matrix with WGP was slightly higher than the nanoscratch hardness.

As mentioned previously, the project area of nanoindentation was much smaller than that of nanoscratch, which means nanoindentation could measure the micromechanical properties of some individual phases, such as CH or glass particles. The nanoscratch hardness was determined according to the scratch depth of the tip under a certain normal load (Rayóna et al. 2018). The difference in test methods made it difficult for the nanoscratch to accurately reflect the hardness of glass particles. For example, when a hemispherical tip touched a small glass particle during scratching, the tip may push it aside rather than swipe directly across the glass. In this condition, the hardness of the combined phase of glass and the surrounding C-S-H would be mistaken for the hardness of the glass particles. As a result, the concordance between nanoscratch hardness and nanoindentation hardness was poor in samples containing WGP.

In general, nanoindentation is likely to reflect the real micromechanical properties of materials, but this is based on a large amount

of test time to produce massive test data, otherwise, it is difficult to observe the right frequency density distribution of mechanical properties (Luo et al. 2018). For materials with high homogeneity, nanoscratch is an ideal technique that can not only ensure the accuracy of test results but also greatly shorten test time (Yin et al. 2022).

## Conclusions

In this study, two groups of MAC samples were prepared to replicate concrete in a simplified manner to avoid the complexities of ITZs in large-scale concrete and improve accuracy in investigating the ITZ. Instead of increasingly scarce conventional SCMs, WGP was used to replace 20% of cement in the sample. The performance of WGP in the ITZ and the adjacent mortar matrix was observed from multiple aspects. The test results obtained from microcharacterization and nanoindentation/nanoscratch were compared and discussed by image analysis or statistical methods. The critical findings can be listed as follows:

- The 20% WGP can greatly reduce the width of ITZ from 30 to 10  $\mu\text{m}$ , featured by the reduction of unreacted cement particles and the increase of hydration products. By contrast, the matrix with WGP had more unhydrated cement particles and fewer hydration products. However, the proportion of pores and cracks was greatly reduced in the ITZ and mortar matrix containing WGP because the WGP participated in the pozzolanic reaction to generate more C-S-H gels, and the unreacted WGP played a role in physically filling pores.
- The cement hydration can be evaluated according to the uniform distribution of Ca and Si elements in EDS mapping. Moreover, the unreacted WGP can also be captured through the distribution of Si and Na elements. In the ITZs without WGP, the Si/Ca ratio of C-S-H was around 0.5. However, when 20% of cement was replaced by WGP, the proportion of C-S-H with a Si/Ca ratio ranging from 1 to 2 was significantly improved, representing a higher cohesion strength.
- XRD and FTIR results showed that the WGP consumed the CH and generated additional C-S-H gels. In addition, the deconvolution results of the FTIR spectrum between 700 and 1,300  $\text{cm}^{-1}$  indicate that the high content of soluble alkali metal oxides in the WGP improved the pH of the pore water, which accelerated the carbonization speed of cement paste and slowed down the formation rate of ettringite.
- The elastic modulus of ITZ and mortar matrix without WGP were in the ranges of 5–20 and 5–23 GPa, respectively, and the frequency density distribution roughly presented a standard normal distribution. However, two relatively independent components appeared in the ranges 10–20 and 19–27 GPa in elastic modulus FDH of ITZ and mortar matrix containing WGP, implying the C-S-H gel and mixed phase of C-S-H and unhydrated or partially hydrated WGP, respectively. The data volume of the nanoscratch was higher than nanoindentation. Low-density C-S-H and high-density C-S-H were found in fracture toughness FDH of ITZ without WGP by deconvolution analysis. In contrast, the distribution of C-S-H in the mortar matrix without WGP was uniform. The ITZ and mortar matrix with WGP can also be separated into two components according to the fracture toughness FDH: C-S-H and a mixed phase of C-S-H and WGP.
- In the comparative analysis of nanoindentation hardness and nanoscratch hardness, nanoindentation results of ITZ and mortar matrix without WGP were consistent with the nanoscratch ones. However, the nanoindentation hardness of ITZs and mortar matrix with WGP was slightly higher than nanoscratch one

because the scratch area of the nanoscratch was much higher than that of nanoindentation. Therefore, nanoscratch is more likely to reflect the mixed nano- and micromechanical properties of multiple phases. For construction materials with high homogeneity, nanoscratch can greatly improve testing efficiency. However, for extremely inhomogeneous materials, the accuracy of nanoindentation was higher based on enough indents.

## Data Availability Statement

All data, models, and code generated or used during the study appear in the published article.

## Acknowledgments

The authors appreciate the support from the Australian Research Council (ARC), Australia (FT220100177, IH200100010, DP220100036, and DP220101051), and the University of Technology Sydney Research Academic Program at Tech Lab (UTS RAPT).

## References

- Akono, A. T., and F. J. Ulm. 2017. "Microscopic toughness of viscous solids via scratching: From amorphous polymers to gas shale." *J. Nanomech. Micromech.* 7 (3): 04017009. [https://doi.org/10.1061/\(ASCE\)NM.2153-5477.0000131](https://doi.org/10.1061/(ASCE)NM.2153-5477.0000131).
- Arabi, N., H. Meftah, H. Amara, O. Kebaïli, and L. Berredjem. 2019. "Valorization of recycled materials in development of self-compacting concrete: Mixing recycled concrete aggregates—Windshield waste glass aggregates." *Constr. Build. Mater.* 209 (Jun): 364–376. <https://doi.org/10.1016/j.conbuildmat.2019.03.024>.
- AS (Australian Standard). 2010. *General purpose and blended cements*. AS 3972. Sydney, Australia: AS.
- AS (Australian Standard). 2014. *Methods for sampling and testing aggregates potential alkali-silica reactivity—Accelerated mortar bar method*. AS 1141.60.1. Sydney, Australia: AS.
- ASTM. 2005. *Standard test method for scratch hardness of materials using a diamond stylus*. ASTM G171-03. West Conshohocken, PA: ASTM.
- ASTM. 2013. *Standard test method for determining the potential alkali-silica reactivity of combinations of cementitious materials and aggregate (accelerated mortar-bar method)*. ASTM C1567-13. West Conshohocken, PA: ASTM.
- del Bosque, I. F. S., W. Zhu, T. Howind, A. Matías, M. I. Sanchez de Rojas, and C. Medina. 2017. "Properties of interfacial transition zones (ITZs) in concrete containing recycled mixed aggregate." *Cem. Concr. Compos.* 81 (Aug): 25–34. <https://doi.org/10.1016/j.cemconcomp.2017.04.011>.
- Diamond, S., and J. Huang. 2001. "The ITZ in concrete—a different view based on image analysis and SEM observations." *Cem. Concr. Compos.* 23 (2–3): 179–188. [https://doi.org/10.1016/S0958-9465\(00\)00065-2](https://doi.org/10.1016/S0958-9465(00)00065-2).
- Dong, W., W. Li, and Z. Tao. 2021. "A comprehensive review on performance of cementitious and geopolymeric concretes with recycled waste glass as powder, sand or cullet." *Resour. Conserv. Recycl.* 172 (Sep): 105664. <https://doi.org/10.1016/j.resconrec.2021.105664>.
- Du, H., and K. H. Tan. 2017. "Properties of high volume glass powder concrete." *Cem. Concr. Compos.* 75 (Jan): 22–29. <https://doi.org/10.1016/j.cemconcomp.2016.10.010>.
- Fang, G., and M. Zhang. 2020. "The evolution of interfacial transition zone in alkali-activated fly ash-slag concrete." *Cem. Concr. Res.* 129 (Mar): 105963. <https://doi.org/10.1016/j.cemconres.2019.105963>.
- Fu, C., Y. Ling, and K. Wang. 2020. "An innovation study on chloride and oxygen diffusions in simulated interfacial transition zone of cementitious material." *Cem. Concr. Compos.* 110 (Jul): 103585. <https://doi.org/10.1016/j.cemconcomp.2020.103585>.

- Garcia-Lodeiro, I., A. Fernandez-Jimenez, M. T. Blanco, and A. Palomo. 2008. "FTIR study of the sol-gel synthesis of cementitious gels: C-S-H and N-A-S-H." *J. Sol-Gel Sci. Technol.* 45 (Jun): 63–72. <https://doi.org/10.1007/s10971-007-1643-6>.
- Garcia-Lodeiro, I., D. E. Macphee, A. Palomo, and A. Fernández-Jiménez. 2009. "Effect of alkalis on fresh C-S-H gels. FTIR analysis." *Cem. Concr. Res.* 39 (3): 147–153. <https://doi.org/10.1016/j.cemconres.2009.01.003>.
- Golewski, G. L. 2018. "An assessment of microcracks in the interfacial transition zone of durable concrete composites with fly ash additives." *Compos. Struct.* 200 (Sep): 515–520. <https://doi.org/10.1016/j.compstruct.2018.05.144>.
- Hjorth, J., J. Skibsted, and H. J. Jakobsen. 1988. "29Si MAS NMR studies of portland cement components and effects of microsilica on the hydration reaction." *Cem. Concr. Res.* 18 (5): 789–798. [https://doi.org/10.1016/0008-8846\(88\)90104-4](https://doi.org/10.1016/0008-8846(88)90104-4).
- Hoover, C. G., and F. J. Ulm. 2015. "Experimental chemo-mechanics of early-age fracture properties of cement paste." *Cem. Concr. Res.* 75 (Sep): 42–52. <https://doi.org/10.1016/j.cemconres.2015.04.004>.
- Hosan, A., F. U. A. Shaikh, P. Sarker, and F. Aslani. 2021. "Nano- and micro-scale characterisation of interfacial transition zone (ITZ) of high volume slag and slag-fly ash blended concretes containing nano SiO<sub>2</sub> and nano CaCO<sub>3</sub>." *Constr. Build. Mater.* 269 (Feb): 121311. <https://doi.org/10.1016/j.conbuildmat.2020.121311>.
- Ismail, Z. Z., and E. A. AL-Hashmi. 2009. "Recycling of waste glass as a partial replacement for fine aggregate in concrete." *Waste Manage.* 29 (2): 655–659. <https://doi.org/10.1016/j.wasman.2008.08.012>.
- Jiang, Y., T. C. Ling, K. H. Mo, and C. Shi. 2019. "A critical review of waste glass powder—Multiple roles of utilization in cement-based materials and construction products." *J. Environ. Manage.* 242 (Jul): 440–449. <https://doi.org/10.1016/j.jenvman.2019.04.098>.
- Ke, G., W. Li, R. Li, Y. Li, and G. Wang. 2018. "Mitigation effect of waste glass powders on Alkali-Silica reaction (ASR) Expansion in cementitious composite." *Int. J. Concr. Struct. Mater.* 12 (7): 1063–1076. <https://doi.org/10.1186/s40069-018-0299-7>.
- Khedmati, M., Y. Kim, and J. A. Turner. 2019. "Investigation of the interphase between recycled aggregates and cementitious binding materials using integrated microstructural-nanomechanical-chemical characterization." *Composites, Part B* 158 (Feb): 218–229. <https://doi.org/10.1016/j.compositesb.2018.09.041>.
- Khedmati, M., Y. R. Kim, J. A. Turner, H. Alanazia, and C. Nguyen. 2018. "An integrated microstructural-nanomechanical-chemical approach to examine material-specific characteristics of cementitious interphase regions." *Mater. Charact.* 138 (Apr): 154–164. <https://doi.org/10.1016/j.matchar.2018.01.045>.
- Kunther, W., Z. Dai, and J. Skibsted. 2016. "Thermodynamic modeling of hydrated white Portland cement–metakaolin–limestone blends utilizing hydration kinetics from 29Si MAS NMR spectroscopy." *Cem. Concr. Res.* 86 (Aug): 29–41. <https://doi.org/10.1016/j.cemconres.2016.04.012>.
- Kunther, W., S. Ferreira, and J. Skibsted. 2017. "Influence of the Ca/Si ratio on the compressive strength of cementitious calcium–silicate–hydrate binders." *J. Mater. Chem. A* 5 (33): 17401. <https://doi.org/10.1039/C7TA06104H>.
- Li, P., W. Li, T. Yu, F. Qu, and V. W. Y. Tam. 2020. "Investigation on early-age hydration, mechanical properties and microstructure of seawater sea sand cement mortar." *Constr. Build. Mater.* 249 (Jul): 118776. <https://doi.org/10.1016/j.conbuildmat.2020.118776>.
- Li, W., Z. Luo, Y. Gan, K. Wang, and S. P. Shah. 2021. "Nanoscratch on mechanical properties of interfacial transition zones (ITZs) in fly ash-based geopolymer composites." *Compos. Sci. Technol.* 214 (Sep): 109001. <https://doi.org/10.1016/j.compscitech.2021.109001>.
- Li, W., J. Xiao, Z. Sun, S. Kawashima, and S. P. Shah. 2012. "Interfacial transition zones in recycled aggregate concrete with different mixing approaches." *Constr. Build. Mater.* 35 (Oct): 1045–1055. <https://doi.org/10.1016/j.conbuildmat.2012.06.022>.
- Lothenbach, B., K. Scrivener, and R. D. Hooton. 2011. "Supplementary cementitious materials." *Cem. Concr. Res.* 41 (12): 1244–1256. <https://doi.org/10.1016/j.cemconres.2010.12.001>.
- Lu, C., Z. Zhang, J. Hu, Q. Yu, and C. Shi. 2022. "Effects of anionic species of activators on the rheological properties and early gel characteristics of alkali-activated slag paste." *Cem. Concr. Res.* 162 (Dec): 106968. <https://doi.org/10.1016/j.cemconres.2022.106968>.
- Lu, J., P. Shen, H. Zheng, B. Zhan, H. A. Ali, P. He, and C. S. Poon. 2020. "Synergetic recycling of waste glass and recycled aggregates in cement mortars: Physical, durability and microstructure performance." *Cem. Concr. Compos.* 113 (Oct): 103632. <https://doi.org/10.1016/j.cemconcomp.2020.103632>.
- Luo, Z., W. Li, V. W. Y. Tam, J. Xiao, and S. P. Shah. 2019. "Current progress on nanotechnology application in recycled aggregate concrete." *J. Sustainable Cem.-Based Mater.* 8 (2): 79–96. <https://doi.org/10.1080/21650373.2018.1519644>.
- Luo, Z., W. Li, K. Wang, A. Castel, and S. P. Shah. 2021. "Comparison on the properties of ITZs in fly ash-based geopolymer and Portland cement concretes with equivalent flowability." *Cem. Concr. Res.* 143 (May): 106392. <https://doi.org/10.1016/j.cemconres.2021.106392>.
- Luo, Z., W. Li, K. Wang, A. Castel, and S. P. Shah. 2022. "Nano/micro-mechanical characterisation and image analysis on the properties and heterogeneity of ITZs in geopolymer concrete." *Cem. Concr. Res.* 152 (Feb): 106677. <https://doi.org/10.1016/j.cemconres.2021.106677>.
- Luo, Z., W. Li, K. Wang, and S. P. Shah. 2018. "Research progress in advanced nanomechanical characterization of cement based materials." *Cem. Concr. Compos.* 94 (Nov): 277–295. <https://doi.org/10.1016/j.cemconcomp.2018.09.016>.
- Lyu, K., E. J. Garboczi, W. She, and C. Miao. 2019. "The effect of rough vs. smooth aggregate surfaces on the characteristics of the interfacial transition zone." *Cem. Concr. Compos.* 99 (May): 49–61. <https://doi.org/10.1016/j.cemconcomp.2019.03.001>.
- Mahmood, A. H., S. Afroz, A. Kashani, T. Kim, and S. J. Foster. 2022. "The efficiency of recycled glass powder in mitigating the alkali-silica reaction induced by recycled glass aggregate in cementitious mortars." *Mater. Struct.* 55 (6): 156. <https://doi.org/10.1617/s11527-022-01989-7>.
- Mejdi, M., W. Wilson, M. Saillio, T. Chaussadent, L. Divet, and A. Tagnit-Hamou. 2019. "Investigating the pozzolanic reaction of post-consumption glass powder and the role of portlandite in the formation of sodium-rich C-S-H." *Cem. Concr. Res.* 123 (Sep): 105790. <https://doi.org/10.1016/j.cemconres.2019.105790>.
- Mejdi, M., W. Wilson, M. Saillio, T. Chaussadent, L. Divet, and A. Tagnit-Hamou. 2022. "Hydration and microstructure of glass powder cement pastes—A multi-technique investigation." *Cem. Concr. Res.* 151 (Jan): 106610. <https://doi.org/10.1016/j.cemconres.2021.106610>.
- Mirzahosseini, M., and K. A. Riding. 2015. "Influence of different particle sizes on reactivity of finely ground glass as supplementary cementitious material (SCM)." *Cem. Concr. Compos.* 56 (Feb): 95–105. <https://doi.org/10.1016/j.cemconcomp.2014.10.004>.
- Mohammadi, I., and W. South. 2016. "The influence of the higher limestone content of General Purpose cement according to high-strength concrete test results and construction field data." *Mater. Struct.* 49 (11): 4621–4636. <https://doi.org/10.1617/s11527-016-0811-y>.
- Mostofinejad, D., S. M. Hosseini, F. Nosouhian, T. Ozbakkaloglu, and B. N. Tehrani. 2020. "Durability of concrete containing recycled concrete coarse and fine aggregates and milled waste glass in magnesium sulfate environment." *J. Build. Eng.* 29 (May): 101182. <https://doi.org/10.1016/j.jobte.2020.101182>.
- Nassar, R. U. D., and P. Soroushian. 2012. "Strength and durability of recycled aggregate concrete containing milled glass as partial replacement for cement." *Constr. Build. Mater.* 29 (Apr): 368–377. <https://doi.org/10.1016/j.conbuildmat.2011.10.061>.
- Omran, A., and A. Tagnit-Hamou. 2016. "Performance of glass-powder concrete in field applications." *Constr. Build. Mater.* 109 (Apr): 84–95. <https://doi.org/10.1016/j.conbuildmat.2016.02.006>.
- Pan, Z., Z. Tao, T. Murphy, and R. Wuhrer. 2017. "High temperature performance of mortars containing fine glass powders." *J. Cleaner Prod.* 162 (Sep): 16–26. <https://doi.org/10.1016/j.jclepro.2017.06.003>.
- Qu, F., W. Li, Y. Guo, S. Zhang, J. L. Zhou, and K. Wang. 2022. "Chloride-binding capacity of cement-GGBFS-nanosilica composites under seawater chloride-rich environment." *Constr. Build. Mater.* 342 (Aug): 127890. <https://doi.org/10.1016/j.conbuildmat.2022.127890>.
- Qu, F., W. Li, K. Wang, S. Zhang, and D. Sheng. 2021. "Performance deterioration of fly ash/slag-based geopolymer composites subjected

- to coupled cyclic preloading and sulfuric acid attack.” *J. Cleaner Prod.* 321 (Oct): 128942. <https://doi.org/10.1016/j.jclepro.2021.128942>.
- Rayóna, E., M. P. Arrieta, T. Pasés, J. López, and J. L. Jordá. 2018. “Enhancing the mechanical features of clay surfaces by the absorption of nano-SiO<sub>2</sub> particles in aqueous media. Case of study on Bronze age clay objects.” *Cem. Concr. Compos.* 93 (Oct): 107–117. <https://doi.org/10.1016/j.cemconcomp.2018.07.005>.
- Scrivener, K. L., A. K. Crumbie, and P. Laugesen. 2004. “The interfacial transition zone (ITZ) between cement paste and aggregate in concrete.” *Interface Sci.* 12 (Apr): 411–421. <https://doi.org/10.1023/B:INTS.0000042339.92990.4c>.
- Tang, Z., W. Li, V. W. Y. Tam, and C. Xue. 2020. “Advanced progress in recycling municipal and construction solid wastes for manufacturing sustainable construction materials.” *Resour. Conserv. Recycl.* 6 (May): 100036. <https://doi.org/10.1016/j.rcrx.2020.100036>.
- Wei, Y., W. Kong, Y. Wang, and A. Sha. 2021. “Multifunctional application of nanoscratch technique to characterize cementitious materials.” *Cem. Concr. Res.* 140 (Feb): 106318. <https://doi.org/10.1016/j.cemconres.2020.106318>.
- Wong, H. S., M. K. Head, and N. R. Buenfeld. 2006. “Pore segmentation of cement-based materials from backscattered electron images.” *Cem. Concr. Res.* 36 (6): 1083–1090. <https://doi.org/10.1016/j.cemconres.2005.10.006>.
- Xiao, J., W. Li, D. J. Corr, and S. P. Shah. 2013a. “Effects of interfacial transition zones on the stress–strain behavior of modeled recycled aggregate concrete.” *Cem. Concr. Res.* 52 (Oct): 82–99. <https://doi.org/10.1016/j.cemconres.2013.05.004>.
- Xiao, J., W. Li, Z. Sun, D. A. Lange, and S. P. Shah. 2013b. “Properties of interfacial transition zones in recycled aggregate concrete tested by nanoindentation.” *Cem. Concr. Compos.* 37 (Mar): 276–292. <https://doi.org/10.1016/j.cemconcomp.2013.01.006>.
- Xu, J., B. Wang, and J. Zuo. 2017. “Modification effects of nanosilica on the interfacial transition zone in concrete: A multiscale approach.” *Cem. Concr. Compos.* 81 (Aug): 1–10. <https://doi.org/10.1016/j.cemconcomp.2017.04.003>.
- Yan, X., H. Zhao, Y. Shen, and H. Ding. 2022. “Material removal mechanism and penetration depth modeling of CF/PEEK composites under nano-scratching.” *Compos. Sci. Technol.* 227 (Aug): 109566. <https://doi.org/10.1016/j.compscitech.2022.109566>.
- Ye, T., J. Xiao, W. Zhao, Z. Duan, and Y. Xu. 2022. “Combined use of recycled concrete aggregate and glass cullet in mortar: Strength, alkali expansion and chemical compositions.” *J. Build. Eng.* 55 (Sep): 104721. <https://doi.org/10.1016/j.job.2022.104721>.
- Yin, Y., Y. Zhao, K. E. Koey, Q. Tan, M. Zhang, and H. Huang. 2022. “In-situ synthesized age-hardenable high-entropy composites with superior wear resistance.” *Composites, Part B* 235 (Apr): 109795. <https://doi.org/10.1016/j.compositesb.2022.109795>.
- Zhan, B., D. Xuan, C. S. Poon, and K. L. Scrivener. 2020. “Characterization of interfacial transition zone in concrete prepared with carbonated modeled recycled concrete aggregates.” *Cem. Concr. Res.* 136 (Oct): 106175. <https://doi.org/10.1016/j.cemconres.2020.106175>.